Geophysical Journal International

Geophys. J. Int. (2024) **237,** 974–988
Advance Access publication 2024 March 6
GJI Applied and Marine Geophysics

https://doi.org/10.1093/gji/ggae086

Indirect joint petrophysical inversion of shallow-seismic and multi-offset ground-penetrating radar field data

Tan Qin,[1,2,3] Thomas Bohlen[3] and Yudi Pan[1,2]

[1]*School of Geodesy and Geomatics, Wuhan University,* 430072 *Wuhan, China. E-mail: yudipan@whu.edu.cn*
[2]*Key Laboratory of Geospace Environment and Geodesy, Ministry of Education, Wuhan University,* 430072 *Wuhan, China*
[3]*Geophysical Institute, Karlsruhe Institute of Technology,* 76187 *Karlsruhe, Germany.*

Accepted 2024 March 5. Received 2024 February 20; in original form 2023 December 12

SUMMARY

In near-surface surveys, shallow-seismic and ground-penetrating radar (GPR) full-waveform inversions (FWIs) have received increasing attention because of their ability to reconstruct high-resolution subsurface models. However, they have different sensitivities to the same targets and thus may yield conflicting geophysical parameter models. To solve this issue, we have developed an indirect joint petrophysical inversion (JPI) integrating shallow-seismic and multi-offset GPR data. These data are used to reconstruct porosity and saturation whereby we use only strong sensitivities between petrophysical and geophysical parameters. To promote its field application, we proposed an input strategy to avoid measuring rock matrix parameters and make indirect JPI more robust. We apply indirect JPI to the field data acquired in Rheinstetten, Germany and find that it reveals the mechanical, electrical and petrophysical properties more reliably than individual inversions. The reconstructed models are assessed by direct-push technology, borehole sample measurements and migrated GPR image. Indirect JPI can fit seismic and GPR observed data simultaneously and provide consistent multiparameter models, which are hard to achieve by FWIs and individual petrophysical inversions. We also find that the method is robust when there are uncertainties in petrophysical *a priori* information. Overall, the field example proves the great potential of using indirect JPI to solve real-world problems.

Key words: Ground penetrating radar; Inverse theory; Joint inversion; Surface waves and free oscillations; Waveform inversion.

1 INTRODUCTION

The near-surface area, a few tens of metres below free surface, are closely related to social development and life safety. A detailed characterization of this area is essential for urban construction, engineering exploration, environmental assessment, archaeological investigation, hydrological monitoring, polar research and so on (Everett 2013; Romero-Ruiz *et al.* 2018; Killingbeck *et al.* 2020). In near-surface surveys, geophysical techniques such as shallow-seismic and ground-penetrating radar (GPR) methods are widely used (Doetsch *et al.* 2020; Leong & Zhu 2021; Liu *et al.* 2022a, b). Shallow-seismic data are sensitive to the mechanical parameters in the subsurface but cannot identify the moisture distribution (Gassmann 1951). GPR data are highly sensitive to the water content, but the depth of penetration is limited by the electrical conductivity (Annan 2005; Bradford & Deeds 2006). Individual inversions of these data may lead to inconsistent interpretations and not fully exploit their advantages. Combining the two data via joint inversion can provide complementary information for each inversion, reducing uncertainty and avoiding ambiguity (Linde *et al.* 2008; Domenzain *et al.* 2022; Moorkamp 2022; Huang *et al.* 2023).

The joint inversion methods can be divided into two main classes: joint structural inversion (JSI) and joint petrophysical inversion (JPI) (Abubakar *et al.* 2012; Linde & Doetsch 2016; Lan *et al.* 2018). JSI assumes that different geophysical parameters have similar spatial distributions (Gallardo & Meju 2011; Feng *et al.* 2017). The cross-gradient function is one of the most commonly used methods to quantify structural similarity (Gallardo & Meju 2003; Jordi *et al.* 2020). On the other hand, JPI supposes that different geophysical parameters are connected via petrophysical relations (Ghose & Slob 2006; Wagner *et al.* 2019). In general, JSI has a broader application than JPI because it does not strictly require accurate *a priori* petrophysical relations. Furthermore, one can make petrophysical inferences based on JSI using methods like the scatter plot (Linde *et al.* 2006; Doetsch *et al.* 2010; Linde & Doetsch 2010). However, the structural constraint (soft link) is weaker than the petrophysical constraint (solid link) (Wagner & Uhlemann 2021). Therefore, JPI is also frequently used, especially in estimating petrophysical

properties such as porosity, saturation and water content (Heincke *et al.* 2017; Wagner *et al.* 2019; Mollaret *et al.* 2020).

JPI is a valuable technique that links all geophysical parameters through their petrophysical relations. However, the applicability of JPI is limited by the accuracy of *a priori* information, including the assumed petrophysical relations and the rock matrix properties. To address this problem, we analysed the sensitivity of shallow-seismic and GPR data to petrophysical parameters and proposed an indirect JPI method (Qin *et al.* 2022). The method indirectly uses petrophysical parametrization so that shallow-seismic and GPR data contribute to porosity and saturation updates, respectively. Compared to the conventional JPI (Abubakar *et al.* 2012), indirect JPI increases the robustness of the inversion under imprecise *a priori* information and thus improves the applicability of the algorithm. We have validated the feasibility and robustness of the algorithm by synthetic examples with different acquisition geometries and wave types (Qin *et al.* 2022), but as of now it has not been used in real cases.

Indirect JPI was developed from full-waveform inversion (FWI) of shallow-seismic and GPR data. FWI is a multiparameter reconstruction technique that exploits the full information content of signals and provides high-resolution multiparameter subsurface models of geological interest (Tarantola 1984). FWI has been extensively developed to solve problems at different scales, in different observation systems, and with different types of waves (Gao *et al.* 2021; Wang *et al.* 2021; Sun *et al.* 2023; Xu *et al.* 2023). In near-surface scale, shallow-seismic wavefield is dominated by Love or Rayleigh waves, which are the result of the interference of SH or *P*–SV waves, respectively. Unlike Rayleigh wave FWI, Love wave FWI has fewer model parameters, lower computational cost and less trade-offs between multiple parameters (Dokter *et al.* 2017; Wittkamp *et al.* 2019). Here, we apply indirect JPI for the first time to Love wave and multi-offset surface GPR field data acquired in the Rheinstetten test site, Germany. We propose an input strategy to make the field application more operational. We compare indirect JPI with single inversions and assess our results with direct-push technology (DPT), borehole sample measurements and GPR migration result. The main goal of this paper is to evaluate the applicability of indirect JPI to solve real-world problems.

2 METHODOLOGY

2.1 Indirect JPI

Indirect JPI is a combination of shallow-seismic and GPR FWIs, where we use the traditional least-squares objective function to quantify the waveform misfit between the observed and synthetic data:

$$\Phi_{\mathrm{S}}(\mathbf{m}_{\mathrm{S}}) = \frac{1}{2}||\mathbf{d}_{\mathrm{S}}^{\mathrm{syn}}(\mathbf{m}_{\mathrm{S}}) - \mathbf{d}_{\mathrm{S}}^{\mathrm{obs}}||^2, \quad \mathbf{m}_{\mathrm{S}} = [V_P, V_S, \rho]^T, \quad s.t. \quad f_{\mathrm{S}}(\mathbf{m}_{\mathrm{S}}, \mathbf{m}_{\mathrm{P}}) = 0, \quad \mathbf{m}_{\mathrm{P}} = [\phi, S_{\mathrm{w}}]^T, \tag{1}$$

and

$$\Phi_{\mathrm{EM}}(\mathbf{m}_{\mathrm{EM}}) = \frac{1}{2}||\mathbf{d}_{\mathrm{EM}}^{\mathrm{syn}}(\mathbf{m}_{\mathrm{EM}}) - \mathbf{d}_{\mathrm{EM}}^{\mathrm{obs}}||^2, \quad \mathbf{m}_{\mathrm{EM}} = [\varepsilon_{\mathrm{r}}, \sigma]^T, \quad s.t. \quad f_{\mathrm{EM}}(\mathbf{m}_{\mathrm{EM}}, \mathbf{m}_{\mathrm{P}}) = 0, \tag{2}$$

where Φ_{S} and Φ_{EM} are the objective functions of shallow-seismic and GPR FWIs, respectively; $\mathbf{d}_{\mathrm{S}}^{\mathrm{obs}}$ is the observed seismogram and $\mathbf{d}_{\mathrm{EM}}^{\mathrm{obs}}$ the observed radargram; $\mathbf{d}_{\mathrm{S}}^{\mathrm{syn}}$ is the synthetic seismogram acquired from the seismic models $\mathbf{m}_{\mathrm{S}}$, and $\mathbf{d}_{\mathrm{EM}}^{\mathrm{syn}}$ is the synthetic radargram acquired from the electromagnetic (EM) models $\mathbf{m}_{\mathrm{EM}}$; $\mathbf{m}_{\mathrm{S}}$ are the *P*-wave velocity V_P, *S*-wave velocity V_S and density ρ; $\mathbf{m}_{\mathrm{EM}}$ are the relative dielectric permittivity ε_{r} and electrical conductivity σ (the magnetic permeability is constant to the value in vacuum and thus is not included). The petrophysical model parameters $\mathbf{m}_{\mathrm{P}}$ are porosity ϕ and saturation S_{w}. The seismic objective function Φ_{S} is subject to the seismic petrophysical relation f_{S}, and the GPR objective function Φ_{EM} is subject to the EM petrophysical relation f_{EM}. In this study, the seismic petrophysical relation f_{S} is Gassmann's equations (Gassmann 1951), and the EM petrophysical relation f_{EM} is the complex refractive index model (CRIM) and Archie's equation (Archie *et al.* 1942; Birchak *et al.* 1974).

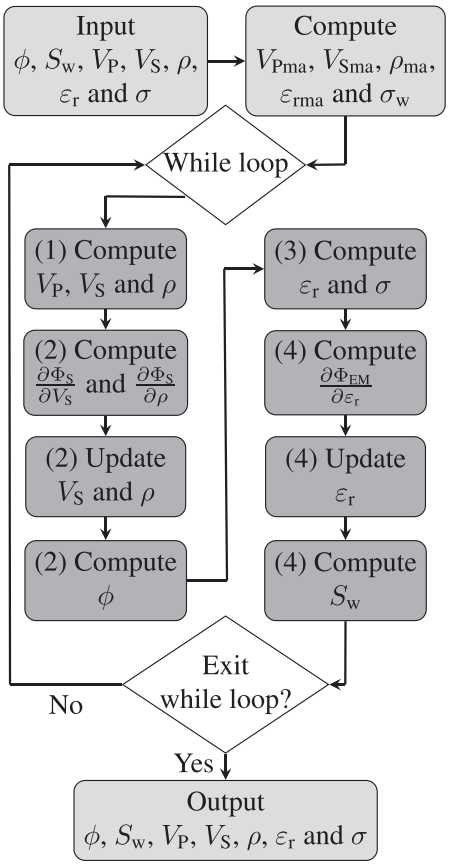

Figure 1. The workflows of indirect joint petrophysical inversion (JPI) with an input strategy. The implementation steps of indirect petrophysical parametrization are indicated by numbers one to four.

Indirect JPI attempts to integrate shallow-seismic and GPR data via separate objective functions (eqs 1 and 2). Like individual FWIs, indirect JPI iteratively updates the model parameters by minimizing the objective functions, for example using the preconditioned conjugate-gradient method (Qin 2022). We implement indirect JPI in each iteration through the following four steps, which we refer to as indirect petrophysical parametrization (Fig. 1).

In step 1, we use Gassmann's equations to calculate the *P*-wave velocity V_P, *S*-wave velocity V_S and density ρ from the petrophysical parameters (Gassmann 1951; Abubakar *et al.* 2012):

$$V_P = \sqrt{\frac{K + 4/3\,\mu}{\rho}}, \qquad V_S = \sqrt{\frac{\mu}{\rho}},$$
$$\rho = (1-\phi)\,\rho_{\mathrm{ma}} + \phi\,[S_{\mathrm{w}}\rho_{\mathrm{w}} + (1-S_{\mathrm{w}})\,\rho_{\mathrm{a}}], \tag{3}$$

with

$$K = (1-\beta)K_{\mathrm{ma}} + \beta^2 M\,, \quad \mu = (1-\beta)\mu_{\mathrm{ma}}\,,$$
$$\frac{1}{M} = \frac{\beta-\phi}{K_{\mathrm{ma}}} + \frac{\phi}{K_{\mathrm{f}}}\,, \quad \frac{1}{K_{\mathrm{f}}} = \frac{S_{\mathrm{w}}}{K_{\mathrm{w}}} + \frac{1-S_{\mathrm{w}}}{K_{\mathrm{a}}}\,,$$
$$K_{\mathrm{ma}} = \rho_{\mathrm{ma}}V_{P\mathrm{ma}}^2 - 4/3\,\mu_{\mathrm{ma}}\,, \quad \mu_{\mathrm{ma}} = \rho_{\mathrm{ma}}V_{S\mathrm{ma}}^2\,,$$
$$\beta = \phi/\phi_{\mathrm{c}} \quad \text{with} \quad 0 \le \phi < \phi_{\mathrm{c}}\,, \tag{4}$$

where K and μ are the bulk and shear moduli of fluid-saturated rock, respectively; ρ_{ma}, ρ_{w} and ρ_{a} are the densities of the rock matrix, water and air, respectively ($\rho_{\mathrm{w}} = 1000\,\mathrm{kg\,m^{-3}}$, $\rho_{\mathrm{a}} = 1.29\,\mathrm{kg\,m^{-3}}$); K_{ma}, K_{f}, K_{w} and K_{a} are the bulk moduli of the rock matrix, pore fluid, water and air, respectively ($K_{\mathrm{w}} = 2.17 \times 10^9$ Pa, $K_{\mathrm{a}} = 1.49 \times 10^5$ Pa); M is the resulting average modulus and μ_{ma} the shear modulus of the rock matrix; $V_{P\mathrm{ma}}$ and $V_{S\mathrm{ma}}$ are the P-wave velocity and S-wave velocity of the rock matrix, respectively; β is the Biot's coefficient and ϕ_{c} the critical porosity. We fix ϕ_{c} to 0.4, above which the solid becomes a suspension (Nur 1992). Thus the range of values for the petrophysical parameters is $0 < \phi < \phi_{\mathrm{c}}$ and $0 < S_{\mathrm{w}} < 1$.

In step 2, we use the seismic velocity parametrization in shallow-seismic FWI to compute the gradients and update the models of V_S and ρ (Köhn *et al.* 2012). The ϕ model is then transformed from the updated V_S and ρ models by using Gassmann's equations as follows:

$$\phi = \phi_{\mathrm{c}}\,(1 - \mu/\mu_{\mathrm{ma}})\,, \quad \mu = \rho V_S^2\,. \tag{5}$$

In step 3, we make ϕ the same size as the GPR models and then use it to calculate the relative dielectric permittivity ε_{r} and electrical conductivity σ by CRIM and Archie's equation (Archie *et al.* 1942; Birchak *et al.* 1974; Day-Lewis *et al.* 2005; Bradford *et al.* 2009):

$$\varepsilon_{\mathrm{r}} = \left\{(1-\phi)\sqrt{\varepsilon_{\mathrm{rma}}} + \phi\left[S_{\mathrm{w}}\sqrt{\varepsilon_{\mathrm{rw}}} + (1-S_{\mathrm{w}})\sqrt{\varepsilon_{\mathrm{ra}}}\right]\right\}^2\,,$$
$$\sigma = \frac{1}{a}\sigma_{\mathrm{w}}\phi^m S_{\mathrm{w}}^n\,, \tag{6}$$

where $\varepsilon_{\mathrm{rma}}$, $\varepsilon_{\mathrm{rw}}$ and $\varepsilon_{\mathrm{ra}}$ are the relative permittivities of the rock matrix, water and air, respectively ($\varepsilon_{\mathrm{rw}} = 81$, $\varepsilon_{\mathrm{ra}} = 1$). σ_{w} is the electrical conductivity of the groundwater, m is the cementation exponent and n is the saturation exponent. a is the tortuosity factor, and is used in practice to correct for data errors or poor petrophysical models, for example using Archie's equation when there is surface electrical conductivity (Linde *et al.* 2006; Revil 2013). Note that in eq. (6), if we fix σ_{w}/a as a constant, different values of a can lead to the same model transformation and thus the same inversion result. In this study, we simply set a to 1.

In step 4, we use the logarithmic parametrization in GPR FWI to compute the ε_{r} gradient and update the ε_{r} model (Meles *et al.* 2010). We then estimate S_{w} by the well-reconstructed GPR model parameter (ε_{r}) through eq. (7), which is another form of CRIM (Birchak *et al.* 1974):

$$S_{\mathrm{w}} = \left\{\left[\sqrt{\varepsilon_{\mathrm{r}}} - (1-\phi)\sqrt{\varepsilon_{\mathrm{rma}}}\right]/\phi - \sqrt{\varepsilon_{\mathrm{ra}}}\right\} / \left(\sqrt{\varepsilon_{\mathrm{rw}}} - \sqrt{\varepsilon_{\mathrm{ra}}}\right)\,. \tag{7}$$

Finally, we make S_{w} the same size as the seismic models and then use it in step 1 in the next iteration.

The main differences of indirect JPI compared to conventional JPI (Abubakar *et al.* 2012) are summarized as below:

(i) We apply non-petrophysical parametrizations (seismic velocity parametrization and logarithmic parametrization) to compute the gradients and update the models of seismic and GPR parameters using their 'natural' model parameters. These parametrizations have proven to be very efficient for shallow-seismic and GPR FWIs (Meles *et al.* 2010; Köhn *et al.* 2012). In contrast, conventional JPI uses petrophysical parametrizations where the gradients of porosity and saturation are given by the chain rule and include the gradients of P-wave velocity and electrical conductivity that are in low reliability and may lead to compromised reconstruction.

(ii) We take the sensitivity of data to seismic and GPR parameters into consideration. Previous studies have shown that shallow-seismic FWI allows high-quality reconstruction of S-wave velocity (Pan *et al.* 2019), and permittivity is the parameter that can be most effectively estimated by GPR FWI (Klotzsche *et al.* 2019). Therefore, we update S-wave velocity and density (density is required to calculate the shear modulus in eq. 5) by shallow-seismic FWI and ignore P-wave velocity, and update permittivity by GPR FWI and ignore electrical conductivity.

(iii) We take into account the sensitivity of seismic and GPR parameters to petrophysical parameters. The sensitivity analysis in Qin *et al.* (2022) suggests that the S-wave velocity and density are mainly affected by porosity, and the permittivity has a relatively strong sensitivity to porosity and saturation (see Fig. 2). Thus we transform the S-wave velocity and density into porosity and transform the permittivity into saturation for efficient information exchange. Note that the last panel in Fig. 2 is a correction to figure 1 in Qin *et al.* (2022), where we forgot to transpose the model matrix when we plotted the electrical conductivity panel. However, this error does not affect the conclusions we have drawn in Qin *et al.* (2022) and in this paper.

(iv) For these hard-to-recover parameters (the P-wave velocity, density and electrical conductivity), we calculate them by petrophysical relations. Since porosity and saturation contain only the most reliable information from shallow-seismic and GPR data, the reconstruction of the P-wave velocity, density and electrical conductivity can be improved, which in turn helps to estimate petrophysical parameters and other seismic and GPR parameters. Thus, we construct a robust joint inversion framework for multiparameter reconstruction.

(v) We use separate objective functions rather than a combined objective function in the joint inversion to avoid calculating the data weighting matrix and the scaling factor (Heincke *et al.* 2017). In indirect JPI, the contribution of shallow-seismic and GPR data is automatically balanced by the sensitivity of the geophysical data to petrophysical parameters. This not only ensures that each data does its job but also reduces the trade-offs of multiparameter inversions. Additionally, this requires as little modification as possible from the individual FWIs to indirect JPI, making the programming of the joint inversion much easier.

In the implementation steps 2 and 4, we consider the sensitivity of shallow-seismic and GPR data to seismic and EM parameters and the sensitivity of seismic and EM parameters to petrophysical parameters. The combination of these sensitivities ensures that the information exchange between the two inversions is not disturbed by the weak-sensitive parameters and thus makes the joint inversion robust.

2.2 Input strategy

In petrophysical inversion, the seismic and EM petrophysical parameters of the rock matrix ($V_{P\mathrm{ma}}$, $V_{S\mathrm{ma}}$, ρ_{ma}, $\varepsilon_{\mathrm{rma}}$ and σ_{w}) are normally assumed to be known, that is *a priori* information (For convenience, we treat the groundwater electrical conductivity σ_{w} also as a rock matrix parameter). However, it is difficult to measure these parameters in the field or in the laboratory. Even more problematic, these parameters are often site-dependent, limiting the

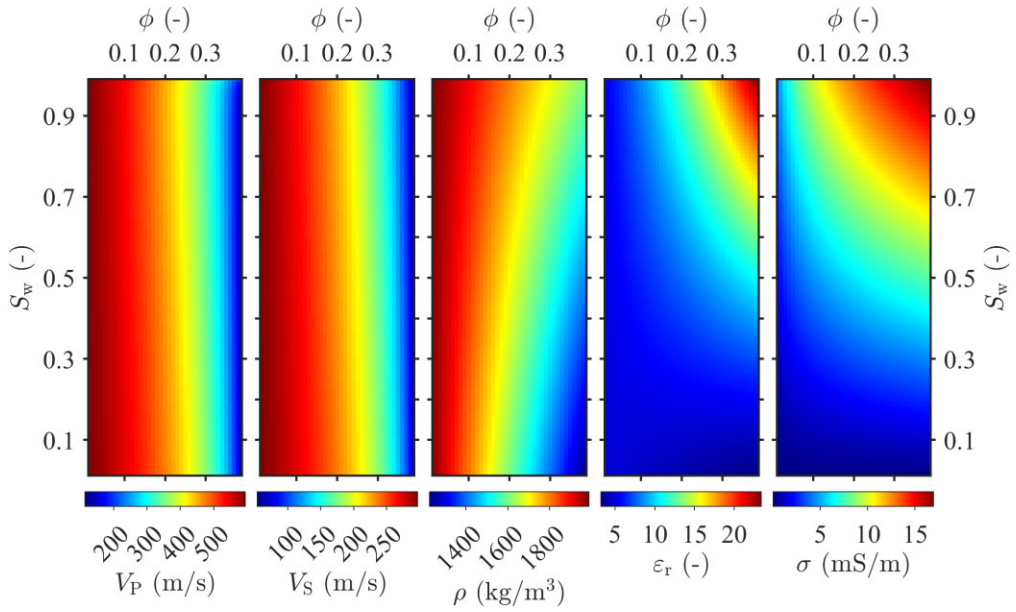

Figure 2. The seismic model parameters (V_P, V_S and ρ) and electromagnetic (EM) model parameters (ε_r and σ) as functions of porosity ϕ and saturation S_w. The rock matrix parameters and Archie's coefficients are the same as Qin *et al.* (2022). Note that the last panel (electrical conductivity) is a correction to figure 1 in Qin *et al.* (2022).

application of petrophysical inversion. To address these issues, we propose an input strategy to calculate the rock matrix parameters at the beginning of JPI (Fig. 1):

$$V_{P\mathrm{ma}} = \sqrt{\frac{K_{\mathrm{ma}} + 4/3\,\mu_{\mathrm{ma}}}{\rho_{\mathrm{ma}}}}\,, \quad V_{S\mathrm{ma}} = \sqrt{\frac{\mu_{\mathrm{ma}}}{\rho_{\mathrm{ma}}}}\,,$$
$$\rho_{\mathrm{ma}} = \{\rho - \phi\,[S_{\mathrm{w}}\rho_{\mathrm{w}} + (1 - S_{\mathrm{w}})\,\rho_{\mathrm{a}}]\}\,/\,(1 - \phi)\,, \tag{8}$$

$$\varepsilon_{\mathrm{rma}} = \left\{\sqrt{\varepsilon_{\mathrm{r}}} - \phi\left[S_{\mathrm{w}}\sqrt{\varepsilon_{\mathrm{rw}}} + (1 - S_{\mathrm{w}})\sqrt{\varepsilon_{\mathrm{ra}}}\right]\right\}^2 / (1 - \phi)^2\,,$$
$$\sigma_{\mathrm{w}} = a\sigma\phi^{-m}S_{\mathrm{w}}^{-n}\,. \tag{9}$$

with

$$K_{\mathrm{ma}} = \left(-b + \sqrt{b^2 - 4dc}\right)/(2d)\,, \quad \mu_{\mathrm{ma}} = \mu/(1 - \beta)\,,$$
$$b = 1/\phi_c - 1 + \beta - K/K_f\,, \quad c = (1 - 1/\phi_c)\,K\,,$$
$$d = (1 - \beta)\,/K_f\,, \quad K = \rho V_P^2 - 4/3\mu\,, \quad \mu = \rho V_S^2\,. \tag{10}$$

Eqs (8) and (9) are another form of the petrophysical relations f_S and f_{EM} when $0 < \phi < \phi_c$ and $0 < S_w < 1$. This input strategy has three advantages:

(i) It avoids measurements of rock matrix parameters and makes indirect JPI more operational in solving practical problems. Using this input strategy, the rock matrix parameters ($V_{P\mathrm{ma}}$, $V_{S\mathrm{ma}}$, ρ_{ma}, $\varepsilon_{\mathrm{rma}}$ and σ_{w}) are implicitly included in the initial models (V_P, V_S, ρ, ε_{r}, σ, ϕ and S_{w}, see Fig. 1). To build these initial models, many classical methods can be used, such as body-wave refraction tomography (V_P), dispersion curve inversion (V_S and ρ), velocity analysis (ε_{r}), amplitude attenuation estimate (σ), measuring the water content of soil samples (ϕ and S_{w}; Xia *et al.* 1999; Annan 2005; Booth *et al.* 2010; Boiero & Socco 2014). Once the initial models are obtained, we use this input strategy to compute the rock matrix parameters and start the iteration of indirect JPI (Fig. 1).

(ii) It makes indirect JPI more robust (see details in Section 3.5). Since shallow-seismic and GPR FWIs rely heavily on seismic and GPR initial models (V_P, V_S, ρ, ε_{r} and σ), it can be expected that indirect JPI can still yield similar results as long as the seismic and GPR models are credible. With this input strategy, empirical estimates based on field conditions can even be used for parameters that have no direct role in shallow-seismic and GPR FWIs, such as porosity, saturation, and Archie coefficients. Thus, indirect JPI can be applied like a single FWI with little limitation of petrophysical *a priori* information.

(iii) It makes indirect JPI also applicable for viscoelastic and dispersive EM media, which are closer to the reality. If the forward solver used to link $\mathbf{d}_S^{\mathrm{syn}}$ and $\mathbf{m}_S$ is viscoelastic equation (Bohlen 2002) or if the forward solver used to link $\mathbf{d}_{\mathrm{EM}}^{\mathrm{syn}}$ and $\mathbf{m}_{\mathrm{EM}}$ is Maxwell's equation in dispersive media (Bergmann *et al.* 1998), $\mathbf{m}_S$ and $\mathbf{m}_{\mathrm{EM}}$ correspond to their values at the reference frequency (Fabien-Ouellet *et al.* 2017; Qin *et al.* 2023) and can be directly used to calculate the rock matrix parameters via eqs (8) and (9).

Note the input strategy also applies to the individual petrophysical inversions (IPIs). For seismic IPI, the rock matrix parameters ($V_{P\mathrm{ma}}$, $V_{S\mathrm{ma}}$ and ρ_{ma}) can be derived from the initial models (V_P, V_S, ρ, ϕ and S_{w}) by eqs (8) and (10). For GPR IPI, the rock matrix parameters ($\varepsilon_{\mathrm{rma}}$ and σ_{w}) can be calculated from the initial models (ε_{r}, σ, ϕ and S_{w}) via eq. (9).

3 APPLICATION TO NEAR-SURFACE IMAGING

3.1 Test site and data acquisition

The data have been acquired at the Rheinstetten test site, Germany, where a V-shaped trench called the Ettlinger Line was excavated in a sedimentary plain covered with gravel and sand from the Rhine river. This trench was refilled with sand a few decades ago and became invisible from the surface at the test site, which is a corner of the glider airfield (Fig. 3a). The current ground layer is composed of partially saturated soil, and the groundwater table is below 6 m depth (Wittkamp *et al.* 2019). From the outcrop in the forest we found that the trench crosses the test site from the northwest to

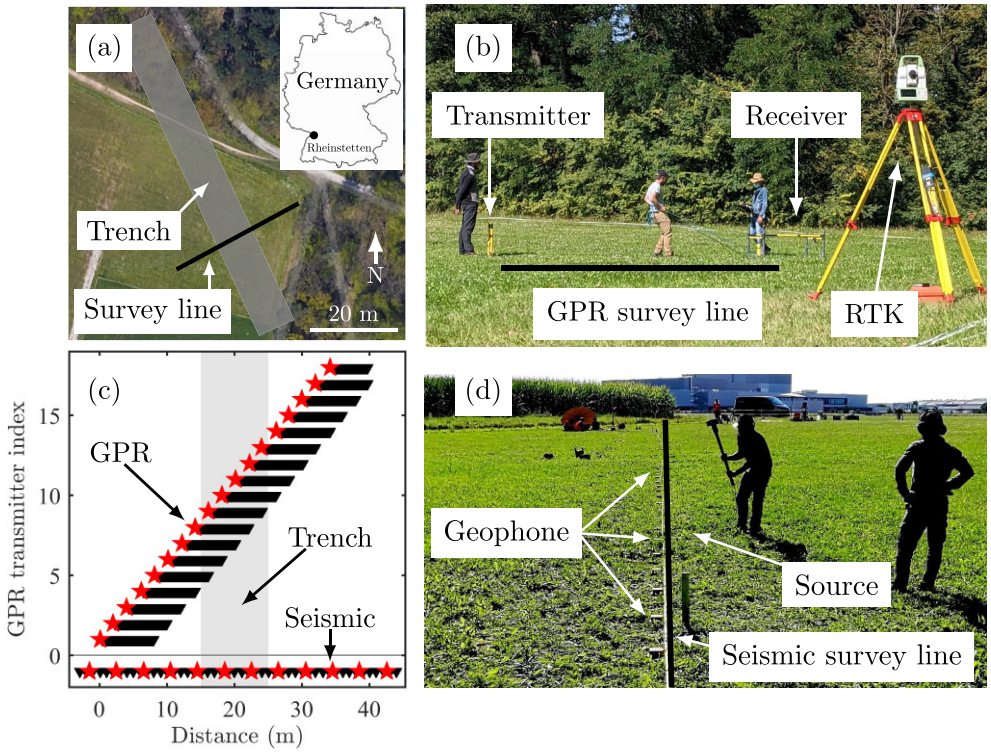

Figure 3. (a) Map of the Rheinstetten test site, where the translucent grey area shows a target trench, the Ettlinger Line, and the black line shows the ground-penetrating radar (GPR) and shallow-seismic survey lines. (b) GPR field data acquisition with the receiver mounted on a sled and tracked by a real-time kinematic (RTK) positioning. (c) Observation geometry of 18 multi-offset GPR data and 12 fixed-spread shallow-seismic data, where the translucent grey area shows the trench location. (d) Shallow-seismic data acquisition using a hammer source and fixed geophone locations.

southeast. We therefore carried out a 2-D investigation with seismic and GPR profiles perpendicular to the Ettlinger Line (Fig. 3a).

To record the Love waves, we deployed 48 geophones (horizontal crossline component) from −3.5 to 43.5 m in the horizontal direction and used a hammer to blow on a steel beam source in the crossline direction (Figs 3c and d). We acquired 12 seismograms with a shot spacing of 4 m and a fixed geophone spread. Our GPR data were recorded using a single channel GPR system with antennas of 200 MHz nominal centre frequency (Figs 3b and c). We deployed the transmitter-receiver orientation in HH mode and acquired 18 radargrams with a transmitter spacing of 2 m. Unlike seismic data acquisition, we used a wide-angle reflection and refraction (WARR) method to acquire the GPR data where we fixed the transmitter and moved the receiver (mounted on a sled) toward or away from the transmitter. To track the receiver coordinates with centimetre-level accuracy, we used a real-time kinematic (RTK) positioning with a self-tracking total station (Boniger & Tronicke 2010).

3.2 Data preprocessing and inversion setup

We pre-process the raw data before using them in the inversion (Table 1).

(i) Since we use the 2-D finite-difference time-domain (FDTD) method to simulate seismic and EM wave propagation (Bohlen 2002; Irving & Knight 2006), we first resample the data to meet the time step requirements of the FDTD methods. This is done by transforming the data to the frequency domain, filling zeros and transforming back to the time domain. After resampling, the time window of the seismogram is 500 ms with a time step of 0.2 ms, and the time window of the radargram is 163.84 ns with a time step of 0.08 ns.

Table 1. Shallow-seismic wave and multi-offset surface GPR data preprocessing steps.

1.	Data resampling in the frequency domain
2.	Interpolation of clipped direct-arrival amplitudes
3.	DC-shift removal and dewow
4.	Bandpass filtering
5.	Bad traces removal and offset limitation
6.	Data gridding in the time-offset domain
7.	3-D-to-2-D transformation

(ii) We use a 1-D spline interpolation to recover the clipped amplitudes of high-energy direct arrivals that exceed the dynamic range of the acquisition unit (Benedetto *et al.* 2017).

(iii) We eliminate low-frequency noise and non-stationary 'wow' noise by mean value removal and dewow operation (Battista *et al.* 2009).

(iv) We apply a Butterworth bandpass filter to remove low- and high-frequency noise. The frequency bandwidth for shallow-seismic data is between 2 and 200 Hz, and for GPR data is between 2 and 400 MHz.

(v) We delete the traces of waveform distortion and remove GPR traces with offsets greater than 8 m because the amplitude of this part is less than two orders of magnitude of the maximum amplitude. For shallow-seismic data, there is no offset limitation because the data are dominated by Love waves and have a high signal-to-noise ratio (SNR).

(vi) After removing bad traces, the data may have irregular trace spacing. Furthermore, in multi-offset GPR data acquisition, the worker moved the sled at an uneven walking speed, which is another reason for the different trace spacing. To ensure a balanced illumination in the measurement area, we apply a 2-D spline interpolation in the time-offset domain with regular trace spacing. After data gridding, seismograms have 46–48 traces with a 1 m trace spacing, and radargrams have 131–192 traces with a 0.04 m trace spacing (Fig. 3c).

(vii) The last preprocessing step before inversion is 3-D-to-2-D transformation which can transform the data recorded in the real world (3-D case) to the 2-D case. This step is important because we implement a 2-D inversion in this study. Based on the wave types contributing to the reconstruction, we use a hybrid 3-D-to-2-D transformation of the direct wave and single wave for shallow-seismic data (Schäfer *et al.* 2014), and a 3-D-to-2-D transformation of the reflected wave for GPR data (Forbriger *et al.* 2014). Note the latter may lead to some errors because the surface GPR data are often dominated by the direct waves (air wave and ground wave).

After preprocessing, the data are ready for the 2-D inversion. We then build initial models based on some data features such as dispersion, travel time and attenuation factor (Fig. 4). The *S*-wave velocity and density initial models are an average of dispersive curve inversion results (Xia *et al.* 2012), and the near-ground values of the permittivity and electrical conductivity are estimated from the velocity and amplitude attenuation of the ground wave (Annan 2005). We assume that the porosity initial model decreases with depth and saturation is a homogeneous half-space (Fig. 5) based on the water content measurement from soil samples (see Section 3.4). We use the cementation exponent $m = 1.4$, and the saturation exponent $n = 1.13$ in Archie's equation where the low values of m and n are chosen for the possible existence of clay, a typical near-surface sediment (Abubakar *et al.* 2012). To account for the attenuation of the *S*-wave velocity, we use a viscoelastic solver with one relaxation mechanism of 40 Hz relaxation frequency and set the attenuation level $Q_S \approx 13.3$. The viscoelastic waves and EM waves are modelled by the 2-D FDTD method (Bohlen 2002; Irving & Knight 2006). We use similar model space but different grid sizes for seismic (0.12 m × 0.12 m) and GPR models (0.04 m × 0.04 m) to simulate them accurately. The convolutional perfectly matched layer (CPML) is included at the model boundaries, except for the free surface of seismic models where an imaging method is applied (Levander 1988). In GPR models, the air layer of 1 m thickness remains constant during the inversion and thus is not displayed (Fig. 4b).

We use a multiscale strategy to avoid cycle skipping in the inversion (Bunks *et al.* 1995). We choose five inversion stages to sequentially use data with ever decreasing wavelength. From the first stage to the fifth stage, frequency bands vary from 5 to 20, 35, 45, 60 and 80 Hz for seismic inversion, and frequency bands vary from 5 to 30, 40, 50, 70 and 100 MHz for GPR inversion. At the beginning of each inversion stage, we estimate the source wavelets with a Wiener filter (Groos *et al.* 2014). The abort criterion is that the relative data misfit change is less than 1 per cent, and the maximum number of iterations per stage is 15. In the joint inversion, the program can switch to the next stage if the abort criteria of both individual inversions are satisfied or if the maximum iteration number is reached. In addition, we apply a 1-D Gaussian filter in the horizontal direction to the gradient to suppress the artefacts shorter than the dominant wavelength.

3.3 Inversion results

The seismic, GPR and petrophysical models reconstructed by indirect JPI successfully reveal the presence of the Ettlinger Line, shown as a triangle anomaly with low *S*-wave velocity, low density, high permittivity and high electrical conductivity values (Fig. 4), resulting from the high porosity and saturation values (Fig. 5). On the one hand, the *S*-wave velocity result is comparable to that of the 3-D shallow-seismic FWIs of Pan *et al.* (2021). On the other hand, the permittivity result is in high agreement with the GPR migration image of Wittkamp *et al.* (2019) and Qin (2022). Due to the constraint of petrophysical relations, the density model also reveals the exact shape of the trench, which is difficult to see from past investigations (Wittkamp *et al.* 2019; Pan *et al.* 2021). For the same reason, the electrical conductivity model has a similar structure to the permittivity model. Note that in the GPR models, the boundaries of the trench become less visible compared to the high permittivity and high electrical conductivity anomalies in the interior. It may result from the high electrical conductivity environment near the surface that degrades the penetration depth of the GPR signal, especially at the bottom of the trench.

Indirect JPI outperforms individual FWIs (Fig. 4). Individual FWIs use the same objective functions (eqs 1 and 2) but are not subject to petrophysical relations. In the seismic model reconstruction, the *S*-wave velocity models estimated by all inversions are very comparable, while the density models reconstructed by seismic FWI show a high-density anomaly inside the trench and a low-density anomaly to the left. Based on the latter DPT and borehole measurements in Section 3.4, these density anomalies could be artefacts caused by the crosstalk from the *S*-wave velocity or by the low sensitivity of Love wave data to density. In comparison, indirect JPI provides significant improvements where there is a low-density triangle anomaly in the middle. When reconstructing the GPR models, individual GPR FWI outlines the shape of the trench, but the model update focuses mainly on the near-surface region (depth shallower than 2 m depth, Fig. 4b). Indirect JPI can update deeper areas and show clearer interfaces.

We compare indirect JPI with IPIs where seismic IPI follows eq. (1), and GPR IPI follows eqs (2). IPIs use petrophysical parametrization to directly update the petrophysical models and then calculate the geophysical models based on the petrophysical relations. Seismic IPI and seismic FWI reconstruct similar *S*-wave velocity models, which implies that Gassmann's equations we used are close to the reality (Fig. 4a). The density model benefits from the petrophysical constraint and shows structures similar to the *S*-wave velocity model. However, the resolution of the density model in seismic IPI is lower than in indirect JPI as the latter is improved by higher resolution GPR data. In terms of GPR IPI (Fig. 4b), the reconstructed models present similar subsurface structures to that of GPR FWI, meaning that CRIM and Archie's equation are also applicable to this test site. Since surface GPR data are dominated by the short-wavelength information, the long-wavelength background models are difficult to update by GPR FWI or IPI alone. To overcome this drawback, joint inversions attempt to use the complementary information from Love wave data. In indirect JPI, seismic data successfully offers the needed information for GPR FWI through the porosity model, thus allowing reconstruction of the low permittivity and low electrical conductivity background. Hence, compared to individual inversions, indirect JPI using more data can constrain the reconstruction process better.

Indirect JPI provides consistent petrophysical models in seismic and GPR inversions. Petrophysical parametrization used in IPIs

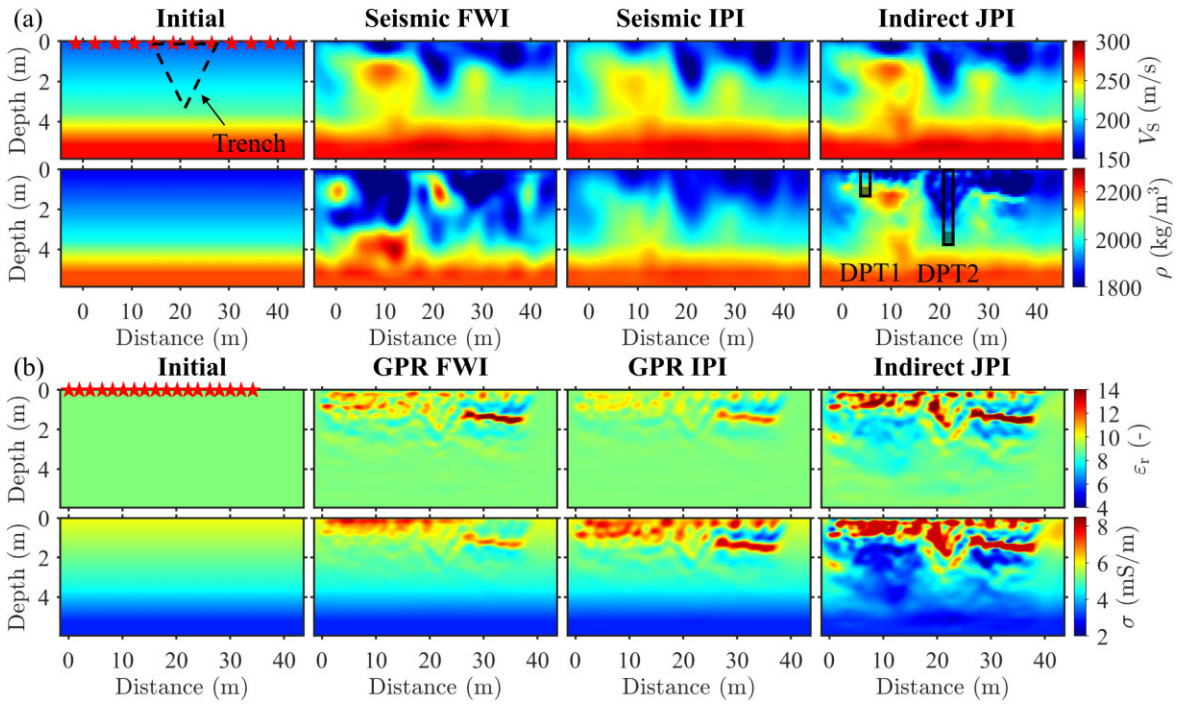

Figure 4. (a) Seismic models (*S*-wave velocity V_S and density ρ) and (b) GPR models (relative permittivity ε_r and electrical conductivity σ). The four columns are the initial models, the reconstructed models of full-waveform inversion (FWI), the reconstructed models of individual petrophysical inversion (IPI), and the reconstructed models of indirect JPI, respectively. In the initial models, the red stars are the sources and the dashed triangle outlines the cross-section of the Ettlinger Line. The borehole histograms overlaid on the density model are the direct-push technology (DPT) results (Figs 7a and b), where the transparent and translucent areas present the unconsolidated and consolidated soil, respectively.

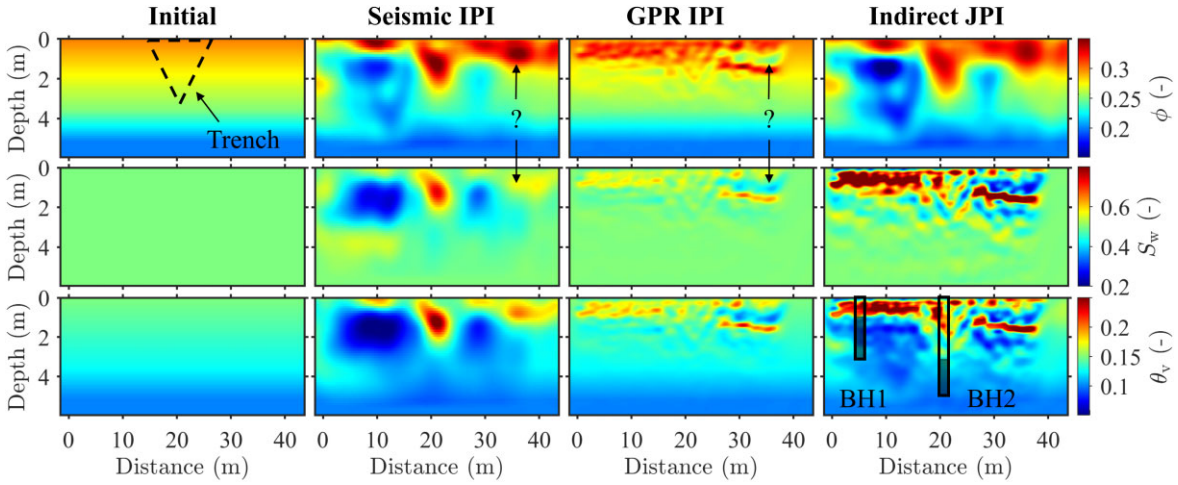

Figure 5. Petrophysical models (porosity ϕ and saturation S_w) and volumetric water content model θ_v. The four columns are the initial models, the reconstructed models of seismic IPI, the reconstructed models of GPR IPI and the reconstructed models of indirect JPI, respectively. The borehole histograms overlaid on the water content model are the gravimetric water content θ_g given by borehole soil samples (Figs 7c and d), where the transparent and translucent areas exhibit high and low water content, respectively.

contains weak sensitivity information, for example electrical conductivity gradient in GPR IPI. Consequently, seismic IPI and GPR IPI generate conflicting results at 0.5–1.5 m depth on the right side of the trench (Fig. 5). Seismic IPI describes this region as high porosity and high saturation anomalies, while GPR IPI interprets it as low porosity and low saturation anomalies. However, indirect JPI characterizes this region as a water-poor layer consisting of high porosity and low saturation anomalies, which proves to be more reliable because in this case we can match both shallow-seismic and GPR data (see Fig. 6).

The seismic and GPR objective functions converge at 35 iterations in indirect JPI. For convenience, we use in the following the relative data misfit, that is dividing the data misfit by that obtained from the initial models (the relative data misfit of the initial models

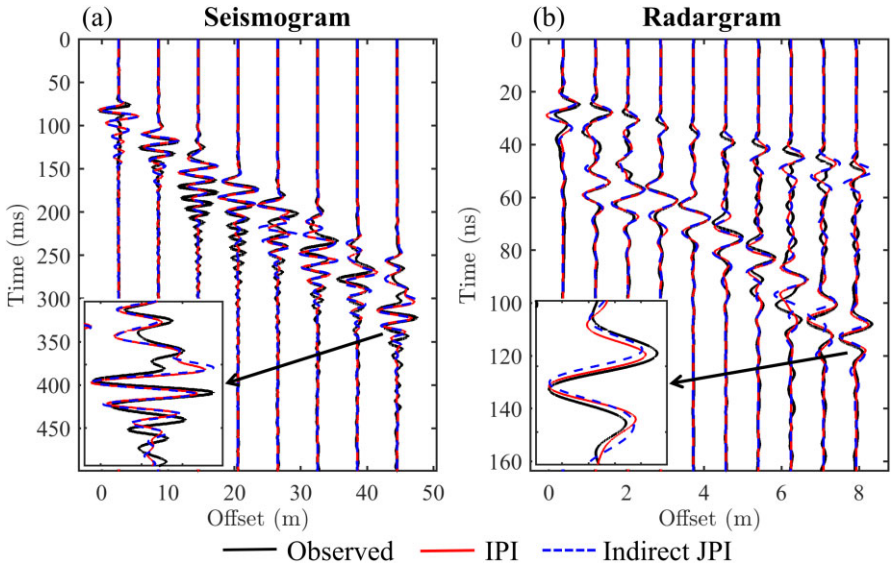

Figure 6. Comparison of the observed data and the synthetic data corresponding to the results of IPI and indirect JPI. (a) The horizontal velocity seismogram of the 1st shot, shown once every six traces. (b) The horizontal electric field radargram of the 16th GPR transmitter, shown once every twenty traces. The rectangular windows display the zoomed waveforms. For better visualization, the data are normalized trace by trace.

is one). To calculate the data misfit of the initial models, we simulate the synthetic data on the initial models with the source wavelet estimated at the last inversion stage and apply the last frequency bandpass filter to the observed data. The GPR data misfit (the relative data misfit is 0.9208) is higher than seismic data misfit (the relative data misfit is 0.8017) due to four reasons. (1) EM waves attenuate much more than seismic waves at the same propagation distance (see figure A2 in Qin *et al.* 2022), thus GPR inversion mainly fits near-offset data, where errors may be greater since the 3-D-to-2-D transformation uses a far-field approximation (Forbriger *et al.* 2014). (2) It is difficult to fit the direct waves in GPR inversions because we use the 3-D-to-2-D transformation of the reflected wave. (3) Our 2-D solver cannot simulate the radiation patterns and antenna-ground coupling well. (4) GPR initial models are quite simple and estimated from the ground wave only, while seismic initial models reference previous studies, which have proven to be useful (Pan *et al.* 2019; Wittkamp *et al.* 2019; Gao *et al.* 2020; Irnaka *et al.* 2022). Overall, the field data fitting could not reach the same good level as the synthetic examples in Qin *et al.* (2022). On the one hand, this is due to the complexity of the field data, lower SNR, higher attenuation, and the influence of the test site, equipment and operators; on the other hand, it is a result of data preprocessing errors, simple initial models and limitations of our forward solvers.

The seismogram fitting of seismic IPI (the relative data misfit is 0.7912) is slightly better than that of indirect JPI (Fig. 6a), and the radargram fitting of GPR IPI (the relative data misfit is 0.9163) and indirect JPI are comparable (Fig. 6b). Overall, the data misfits of indirect JPI are slightly higher than that of seismic and GPR IPIs (about 1 and 0.4 per cent, respectively) because of the interaction of seismic and GPR data and the additional petrophysical constraint. However, neither seismic IPI nor GPR IPI can minimize the two data misfits simultaneously. For example, we use the petrophysical models reconstructed by seismic IPI to derive GPR models (eq. 6) and perform a GPR forward modelling on them; we then use the simulated GPR data to calculate the data misfit and find that it is much higher than that of indirect JPI, and vice versa. From this perspective, indirect JPI is a better way to fit seismogram and radargram at the same time, leading the seismic and GPR model update in an acceptable direction for both.

3.4 Assessment

To evaluate our interpretations of the density model, we compare the inversion results with two independent DPT measurements (see Figs 4a, 7a and b). In DPT measurements, a metal pile was hit by a free-falling slide hammer (10 kg) and thus pushed into the ground. By recording the number of hits per 0.1 m depth pushed in, we measured the consolidation degree in the subsurface. The higher the number, the more compact the soil. We have one DPT measurement outside the trench (DPT1) and another one inside the trench (DPT2). These DPT measurements reveal a change from loose topsoil (lower density) to compacted subsoil (higher density) at 1 m depth at the DPT1 position and an interface between refilled sand (lower density) and underlying soil (higher density) at 3 m depth at the DPT2 location, which corresponds to the bottom of the trench (Figs 7a and b). These findings agree with the density model of seismic IPI and indirect JPI and prove that petrophysical constraint improves the density reconstruction.

To assess the water content given by petrophysical inversions, we drilled two boreholes (BH1 and BH2) close to the DPT locations and collected soil samples every 0.5 m depth (Fig. 5). We then measured the gravimetric water content θ_g of the soil samples by drying them in the laboratory. The borehole measurements show a change in water content at similar depths to the DPT results. For convenience, we convert the petrophysical inversion result to the gravimetric water content by $\theta_g = \theta/(1-\theta)$, where $\theta = \theta_v/\rho$ and the volumetric water content $\theta_v = \phi S_w$. In GPR IPI, we use the density of seismic IPI to calculate θ_g. Note that the uncertainties present in the density may affect the conversion from θ_v to θ_g. We find that indirect JPI fits well with the BH1 measurement in both high and low water content area (Figs 5 and 7c). For BH2, seismic IPI overestimates the water content in the trench, and GPR IPI underestimates it and shows result very close to the initial model

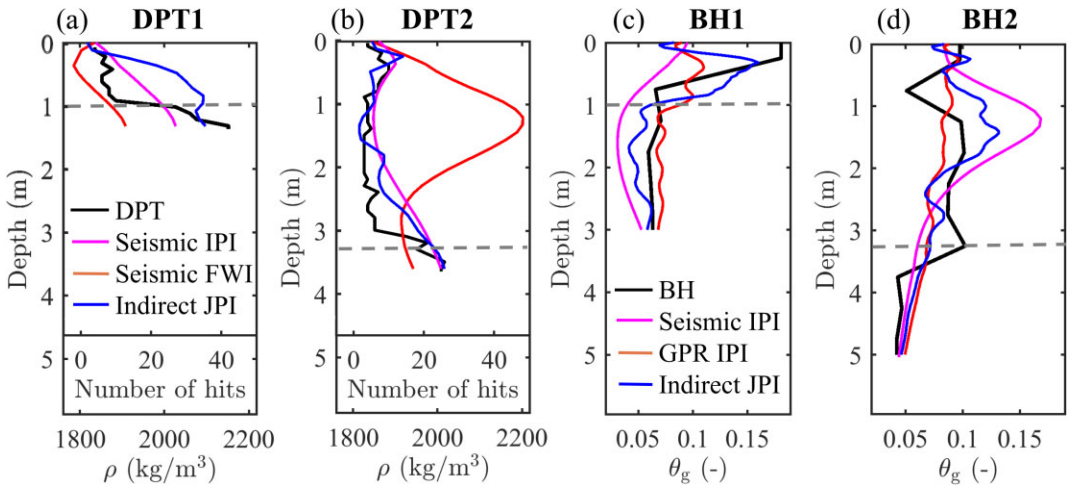

Figure 7. Comparison of inversion results, DPT, and borehole measurements. The black lines in (a) and (b) are the number of hits measured by DPT, and the black lines in (c) and (d) are the gravimetric water contents (θ_g) of borehole soil samples. The colourful lines are the inversion results, that is density in (a) and (b) and θ_g in (c) and (d). The gray dashed lines mark the interfaces between transparent and translucent areas of the borehole histograms shown in Figs 4 and 5.

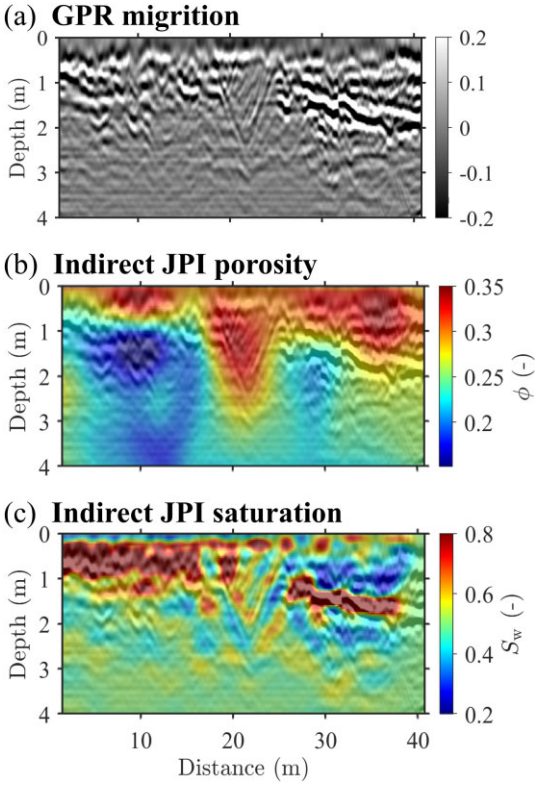

Figure 8. Comparison between (a) the migration result of common-offset GPR data, (b) the porosity and (c) saturation results of indirect JPI. The colour scale of (a) is clipped to 20 per cent of the highest amplitude for better visualization. In (b) and (c) we overlay the migration image on the petrophysical models.

(Figs 5 and 7d). Indirect JPI's result is better than seismic IPI's result, although further improvements are needed.

We compare the indirect JPI results with the GPR migration result along the same profile (Fig. 8). After performing a classical GPR processing including bandpass filtering (50–400 MHz), zero-time correction, time-dependent scaling, we apply a Kirchhoff migration routine (Moran *et al.* 2000) to the common-offset data (offset = 0.5 m) using a constant subsurface velocity of 0.1 m ns^{-1}. The migrated GPR image shows the trench in the centre and the dipping high amplitude reflector on the right-hand side of the trench (Fig. 8a). The migrated data on the left-hand side of the trench appear more chaotic, with a lower penetration depth. For better comparison, we overlay the migration image on the indirect JPI results (Figs 8b and c). We find that the migration image agrees well with the porosity and saturation images in terms of the location and structures of the Ettlinger Line and the right-hand reflector. Therefore, we conclude that indirect JPI is capable of reconstructing the petrophysical models with high reliability, especially for shallow subsurface structures.

3.5 Robustness tests

It is well known that the performance of petrophysical inversions tends to depend on *a priori* information, that is the rock matrix parameters and Archie's coefficients in this study. To evaluate the inversion robustness, we take the mean structural similarity (MSSIM) index to measure the fidelity of the reconstructed models of indirect JPI using different petrophysical initial models and Archie's coefficients relative to the reference. We adopt the same settings as Boniger & Tronicke (2010) to compute the MSSIM index. The closer the MSSIM index is to one, the more similar the two compared objects are. Instead of giving the rock matrix parameters explicitly, we compute them from the initial models via the input strategy (eqs 8 and 9). Therefore if we fix seismic and GPR initial models, the rock matrix parameters can be changed either by petrophysical initial models (porosity and saturation) or by Archie's coefficients.

We take the indirect JPI shown in Fig. 5 as the reference and other four indirect JPIs using homogeneous petrophysical initial models in half-space for comparison (Fig. 9). When we change petrophysical initial models to different values ($\phi = 0.2$ or 0.3 and $S_w = 0.5$ or 0.7), the reconstructed seismic and GPR models present a high degree of structural similarity to the reference (see MSSIM index in Fig. 9). Compared to the GPR models, the seismic models are reconstructed very stably (all MSSIM indices are greater than 0.985) because they are influenced only by porosity, whereas the GPR

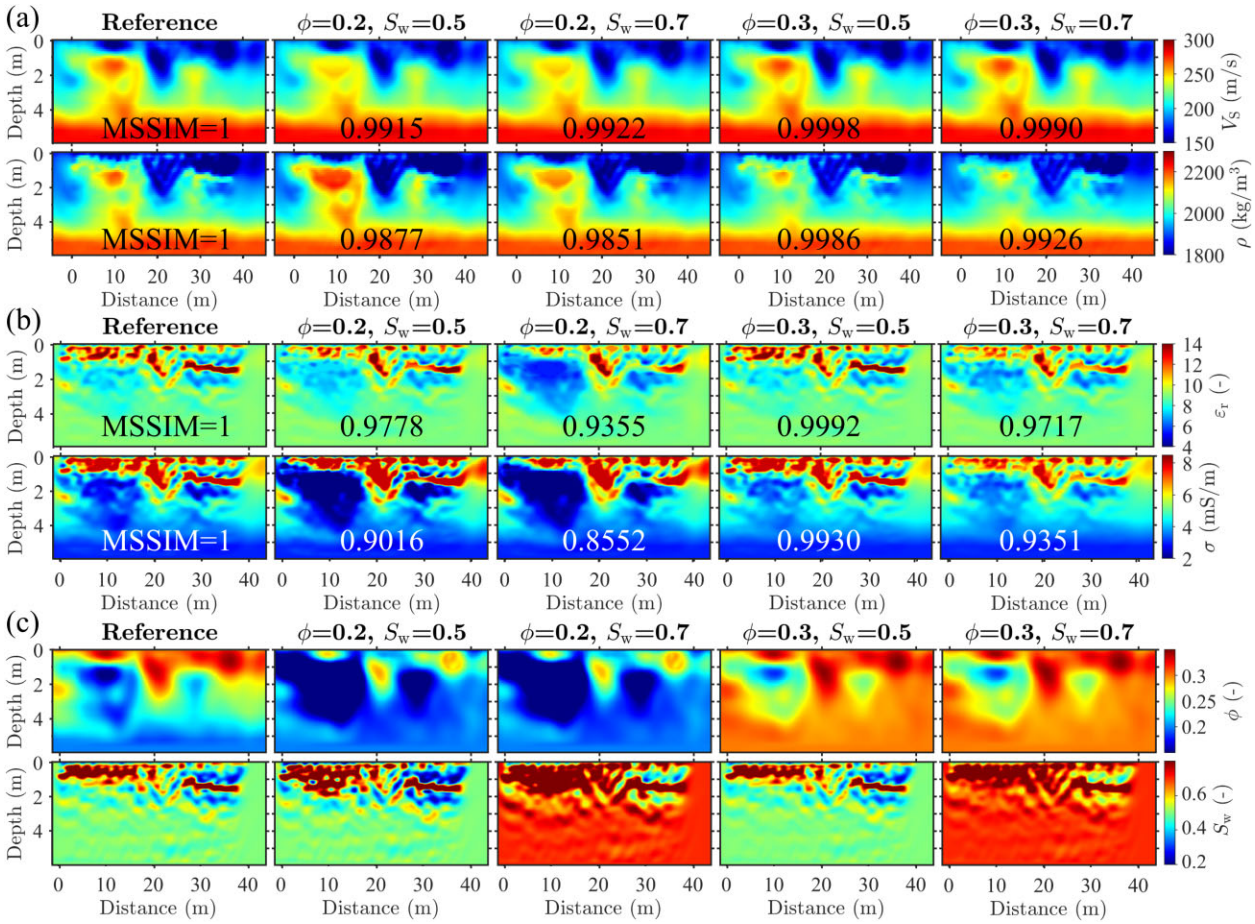

Figure 9. (a) Seismic models (*S*-wave velocity V_S and density ρ), (b) GPR models (relative permittivity ε_r and electrical conductivity σ) and (c) petrophysical models (porosity ϕ and saturation S_w). The five columns are the indirect JPI results with different petrophysical initial models (see the title of each row). These five JPIs have the same seismic and GPR initial models as in Fig. 4. The referenced petrophysical initial models are the same as in Fig. 5. The values overlaid on the models in (a) and (b) are the mean structural similarity (MSSIM) index relative the reference.

models are affected by both porosity and saturation. The results of $\phi = 0.3$ generally have higher structural similarity than those of $\phi = 0.2$ because the near-ground values of the reference porosity model are close to 0.3 and shallow-seismic and GPR data are more sensitive to shallow than deep zones. With $\phi = 0.2$ and $S_w = 0.7$, we observe the largest differences in permittivity (MSSIM = 0.9355) and electrical conductivity (MSSIM = 0.8552). However, even in this case, all models can delineate consistent subsurface structures and provide a meaningful geological interpretation. Note that there are significant differences between the petrophysical models reconstructed with different petrophysical initial models. Among them, the reference model best matches the gravimetric water content of the borehole soil samples (Figs 7c and d) because its initial model allows for the trend of decreasing water content with depth (Fig. 5). Therefore, we recommend building the petrophysical initial models based on the borehole data if they are available. If not available, an empirical guess of the petrophysical initial models is acceptable for indirect JPI, but the geological interpretation should be based primarily on the reconstructed seismic and GPR models.

We test indirect JPI with the same initial electrical conductivity model (Fig. 4b) but different Archie's coefficients, corresponding to different groundwater electrical conductivities (eq. 9). The range of m between 0.4 and 2.4 and n between 1.13 and 3.00 gives almost identical results (MSSIM > 0.99, see Fig. 10). In other words, the choice of Archie's coefficients has a negligible impact on indirect JPI's performance. This should be attributed to the abandonment of weakly sensitive electrical conductivity information in indirect petrophysical parametrization and to the indirect calculation of the groundwater electrical conductivity in the input strategy (Fig. 1).

Overall, these examples demonstrate that indirect JPI does not need to know accurate *a priori* information. With suitable seismic and GPR initial models, any petrophysical initial models and Archie's coefficients in a reasonable range can produce similar results. This strength makes indirect JPI a robust and promising technique that could be easily applied to other field environments with as few assumptions about petrophysical relations as possible.

4 DISCUSSION

4.1 New scientific findings

This is a follow-up work to Qin *et al.* (2022) that performed the theoretical study and synthetic test on indirect JPI. The major novelty of this work is that we assessed the feasibility of our algorithm

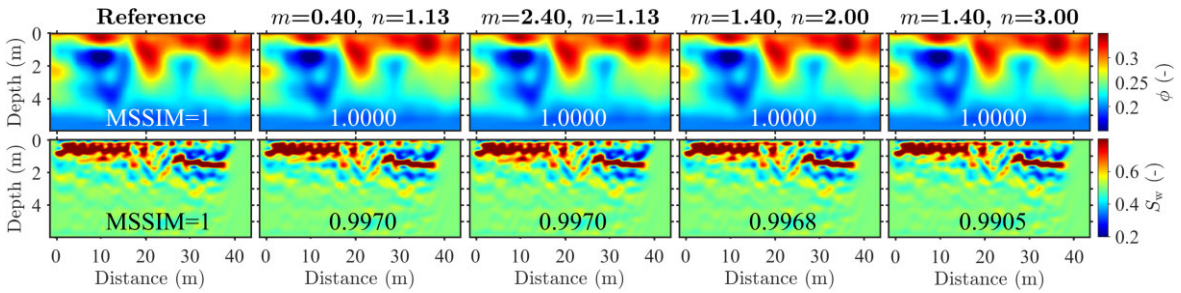

Figure 10. Petrophysical models (ϕ and S_w). The five columns are the indirect JPI results with different Archie's coefficients (cementation exponent m and saturation exponent n). The initial models of five JPIs are the same as the reference in Fig. 9. The values overlaid on the models are the MSSIM index relative to the reference ($m = 1.4$ and $n = 1.13$).

in solving practical problems. To facilitate the field application, we combined indirect JPI with an input strategy that avoids the measurement of the rock matrix parameters, making the algorithm more robust and suitable for complicated environments. Comparison with the three third-party methods showed that the results of indirect JPI are of higher quality than those of FWI and IPI. Note that the robustness tests are different from those in Qin *et al.* (2022), where we keep the petrophysical initial models unchanged and perturb the rock matrix parameters (or Archie's coefficients), causing changes in the seismic and GPR initial models and thus having a greater impact on the reconstruction results. In this study, we leave the seismic and GPR initial models fixed, but adopt the input strategy to change the rock matrix parameters by petrophysical initial models or by Archie's coefficients. Shallow-seismic and GPR FWI mainly depend on the seismic and GPR initial models, so indirect JPI in this study suffers less from inaccurate petrophysical *a priori* information than in the previous study.

Indirect JPI is an algorithm different from conventional JPI. Conventional JPI is a combination of two IPIs in which the petrophysical parameters are reconstructed by the chain rule based on petrophysical relations (Abubakar *et al.* 2012). Conventional JPI merges all the information from two geophysical data and tends to obtain a compromise between the two IPIs. In contrast, indirect JPI integrates two FWIs to update seismic and GPR parameters, and then indirectly transforms the results into petrophysical parameters using petrophysical relations. This is why we call it indirect petrophysical parametrization. The stable performance of the algorithm should be attributed to the rational use of petrophysical sensitivity, non-petrophysical parametrizations and the input strategy (Fig. 1). Taking into account the sensitivity differences of geophysical data to petrophysical parameters ensures a highly efficient exchange of information between two geophysical inversions. Seismic velocity parametrization and logarithmic parametrization fully exploit the reconstruction potential of shallow-seismic and GPR FWI, respectively. The input strategy reduces the difficulty of using petrophysical inversion and makes indirect JPI less dependent on petrophysical initial models and petrophysical relations. The integration of the above three parties makes indirect JPI a robust algorithm that may be applied to the field data. Hence, indirect JPI overcomes the bottleneck of conventional JPI and provides a new way for JPI development.

The motivation of this study is to answer the questions about geophysical inversion: Can we use JPI to improve the reconstruction result and avoid conflicting interpretations? Is it possible to easily apply JPI to field data? The first question is a basic requirement for all joint inversion studies, and our answer is yes. The field example revealed that indirect JPI can better use the strengths of shallow-seismic and GPR data and produce results much better than individual inversions. The second question is challenging for petrophysical inversion because the assumed petrophysical relations and *a priori* information may be site-dependent and hard to obtain. However, our study indicated that indirect JPI still has a stable performance when there are uncertainties in *a priori* information. Indirect petrophysical parallelization, in combination with the input strategy, makes the field data application of JPI possible and promising. Therefore, our answer to the second question is yes, and we believe indirect JPI deserves more attention.

4.2 Limitations of indirect JPI

The petrophysical parameters we consider in this study are porosity and saturation (water content is their product), which are the objects of most petrophysical inversions. In some cases, it may be necessary to include other petrophysical parameters, for example clay content. Clay content is a key factor affecting seismic and EM properties. For instance, electrical conductivity is controlled by clay content and groundwater electrical conductivity. Although we attempted to use low values of m and n to account for the presence of clay, the adopted Archie's equations may not be the best choice because it was derived from a clay-free matrix (Archie *et al.* 1942). A possible solution is to use petrophysical relations that can consider the effect of clay content on seismic and EM parameters, such as the Voigt–Reuss–Hill (VRH) boundary model and Linde's modification of Archie's equation (Linde *et al.* 2006; Hu *et al.* 2021). Additionally, electrical resistivity data are sensitive to electrical conductivity and may be introduced into the joint inversion to reconstruct the clay content model. In this way, indirect JPI can be extended from two to three geophysical data based on the sensitivity links between shallow-seismic data and porosity, GPR data and saturation, and electrical resistivity data and clay content.

Non-petrophysical parametrizations is another key factor affecting indirect JPI's performance. Seismic velocity parametrization has proven to be very beneficial for seismic multiparameter imaging, mainly due to the similarity in magnitude of seismic velocity and density (Köhn *et al.* 2012). Nevertheless, seismic modulus parametrization may also be worth a try since we actually use the shear modulus to calculate porosity (eq. 5). In seismic velocity parametrization, the shear modulus is calculated from the *S*-wave velocity and density, and may be contaminated by less reliable density information. Whereas, in seismic modulus parametrization, the shear modulus is updated only by the shear modulus gradient

without any interferences, and thus may be more reliable. Therefore, indirect JPI with seismic modulus parametrization instead of seismic velocity parametrization may yield better results, which is subject to further validation.

As the first step, we evaluated our algorithm via Love wave and multi-offset surface GPR field data. As shown in table 2 in Qin *et al.* (2022), there are 12 combinations of geometries (crosshole and surface) and wave types (*P*–SV, SH, TE and TM) in the 2-D case. Therefore, other combinations need to be tested in the next studies. What we can expect is that indirect JPI with *P*–SV wave (Rayleigh wave) will be more challenging since more parameters have to be reconstructed, and the crosshole geometry will illuminate better in deeper area than surface geometry. Applying indirect JPI in the 3-D case will be the next step.

The current version of indirect JPI does not include model regularization. Model regularization is an effective way to stabilize the inversion process and improve the imaging results (Tikhonov & Arsenin 1977). For example, the maximum smoothness regularization (Constable *et al.* 1987) may constrain the horizontal roughness and suppress artefacts in the near-surface GPR models (Fig. 4b); the total variation regularization (Feng *et al.* 2019) may make the trench boundaries and other subsurface interfaces in the seismic models sharper (Fig. 4a). Therefore, indirect JPI combined with model regularization is worth further investigation.

4.3 Implications of the work

The workflow we propose in Fig. 1 can be regarded as a general framework of joint inversion. It is a way to stabilize the reconstruction process and exchange the most reliable information from each data. Our study motivates the consideration of sensitivity difference and the use of non-petrophysical parametrization in the joint inversion. In near-surface survey, indirect JPI of shallow-seismic and electrical resistivity data can be developed similarly by replacing GPR FWI with electrical resistivity inversion and calculating saturation from electrical conductivity based on Archie's equation (Wagner *et al.* 2019). GPR and electrical resistivity data can be integrated by indirect JPI as well (Domenzain *et al.* 2020), where the frequency difference in the electrical conductivity reconstructed by two inversions should be taken into account (Qin *et al.* 2023). In oil exploration, one can perform indirect JPI of seismic and controlled-source electromagnetic measurements (CSEM) data, namely, replacing GPR FWI with CSEM inversion and computing saturation from electrical conductivity (Abubakar *et al.* 2012). Note that it is possible to calculate porosity from *P*-wave velocity since seismic FWI uses mainly reflected waves and is also sensitive to *P*-wave velocity in oil exploration. Furthermore, JPI is not limited to the traditional framework of using only petrophysical parametrizations. Our study indicates that using non-petrophysical parametrization in JPI can better exploit the reconstruction potential of FWI. Thus, indirect JPI holds great promise as a generalized framework that may be applied to a wide range of joint inversion studies.

The approach presented is not limited to the empirical models given by Gassmann's equations, CRIM and Archie's equation. It is also applicable to other petrophysical relations. For example, the time-averaging equation can be used for the seismic petrophysical relation f_S (Wagner *et al.* 2019), and Topp's equation and Ewing's modification of Archie's equation can be taken as the EM petrophysical relation f_{EM} (Topp *et al.* 1980; Ewing & Hunt 2006). Some petrophysical relations reveal similar sensitivity trend as Fig. 2, for example the permittivity increases with porosity and saturation in CRIM and Topp's equations. Indirect JPI using these petrophysical relations is expected to give similar results as in this study. For petrophysical relations with different sensitivity trends, such as Gassmann's equations and the time-averaging equation, indirect JPI may have a stable performance but different results. However, how to judge whether the adopted relations are valid for the test site is an open question. As an attempt, we suggest to implement FWI and IPI first. If their results are similar (e.g. *S*-wave velocity in Fig. 4), the petrophysical relations are close to the real situation in the test site, and then we can run indirect JPI using these petrophysical relations. If the results of FWI and IPI are far apart, other petrophysical relations should be tested until the most suitable one is found. An alternative is to use JSI to derive possible petrophysical relations from a scatter plot of multiple geophysical parameters (Linde & Doetsch 2010), for example *S*-wave velocity and permittivity reconstructed by seismic and GPR FWIs. This deserves further investigation.

The computational cost of the joint inversion is the sum of two individual inversions. In this paper, we run our algorithm on a 36-core computer cluster. Shallow-seismic FWI has 12 seismograms (2500 sampling rate) and model space 412 $\times$ 50 grids, simulated with 12 source parallelization and three model domain parallelization (one model decomposed into three subvolumes) (Bohlen 2002). GPR FWI has 18 radargrams (2048 sampling rate) and model space 1130 $\times$ 175 grids, simulated with 18 source parallelization and two model domain parallelization. We use a subset FWI (SFWI) method to speed up GPR FWI by a factor of five and reduce the memory usage to 20 per cent (Qin 2022). As a result, the total computational time of indirect JPI is about nine minutes. The computational cost can be further reduced by applying the source encoding method to shallow-seismic FWI and GPR FWI (Krebs *et al.* 2009; Feng *et al.* 2023). However, GPR data acquisition requires special attention because each data has an unfixed geometry spread. To make source encoding applicable to GPR data acquisition and to eliminate the crosstalk of uncorrelated wavefields, frequency-division encoding method may be considered (Huang & Schuster 2012).

5 CONCLUSION

In this paper, we applied indirect JPI to shallow-seismic and multi-offset surface GPR field data for consistent imaging of the near-surface targets. Indirect JPI exploits only highly sensitive relations between geophysical and petrophysical parameters. In this case these relations are *S*-wave velocity $\propto$ porosity and permittivity $\propto$ saturation. We proposed an input strategy to make indirect JPI more operational and robust in solving practical problems. The application at the Rheinstetten test site showed that this approach not only outperforms FWIs and IPIs in reconstructing seismic and GPR parameters, but also provides more consistent petrophysical models than IPIs. Indirect JPI presented significant improvements in estimating saturation, density, and electrical conductivity, therefore reducing the ambiguity and uncertainty of single geophysical techniques and facilitating the final geological interpretations, such as determining groundwater distribution and facies stratification. This study also suggested that, due to the use of indirect petrophysical parametrization, this approach can efficiently exchange the high confidence information given by each inversion. Thanks to the separate contributions of seismic and GPR data, indirect JPI reduced the reliance on *a priori* information and exhibited great potential for

real-world applications. Our observations are in agreement with the DPT, borehole measurements and GPR migration image. To sum up, this study is the first application of indirect JPI to field data and the results are promising.

ACKNOWLEDGMENTS

This work is financially supported by the China Scholarship Council (No. 201806260258), the Natural Science Foundation of Hubei Province (No. 2023AFB114), the China Postdoctoral Science Foundation (No. 2023M742683) and the Fundamental Research Funds for the Central Universities with project number 2042023kfyq01. Tan Qin would like to thank Tilman Steinweg and Mark Wienöbst for their help in developing the WAVE-Toolbox. The authors sincerely thank Lars Houpt, Felix Bögelspacher, Michael Mayer, Hagen Steger, Roland Helfer and the master students at Geophysical Institute, Karlsruhe Institute of Technology for their help in field data acquisition. The GPR data have been acquired with the equipment of the University of Potsdam and the valuable help of Niklas Allroggen and Philipp Koyan. The authors thank the editor, Dr. Rene-Edouard Plessix, and two anonymous reviewers for their constructive comments.

DATA AVAILABILITY

The field data and synthetic models used in this work can be obtained from the KITopen repository (https://doi.org/10.35097/1709). An open-source software (GPL) package containing the source code used in this paper is provided in the WAVE-Toolbox (https://github.com/WAVE-Toolbox). Version 1.0 of the WAVE-Toolbox used for this study is archived at the Zenodo repository (https://doi.org/10.5281/zenodo.6875824 and https://doi.org/10.5281/zenodo.6875830).

REFERENCES

Abubakar, A., Gao, G., Habashy, T.M. & Liu, J., 2012. Joint inversion approaches for geophysical electromagnetic and elastic full-waveform data, *Inverse Problems,* **28**(5), doi:10.1088/0266-5611/28/5/055016.

Annan, A.P., 2005. GPR methods for hydrogeological studies, in *Hydrogeophysics,* Vol. **50,** pp. 185–213, Rubin, Y. & Hubbard, S.S., Springer.

Archie, G.E. *et al.*, 1942. The electrical resistivity log as an aid in determining some reservoir characteristics, *Trans. AIME,* **146**(01), 54–62.

Battista, B.M., Addison, A.D. & Knapp, C.C., 2009. Empirical mode decomposition operator for dewowing GPR data, *J. Environ. Eng. Geophys.,* **14**(4), 163–169.

Benedetto, A., Tosti, F., Ciampoli, L.B. & D'amico, F., 2017. An overview of ground-penetrating radar signal processing techniques for road inspections, *Sig. Process.,* **132,** 201–209.

Bergmann, T., Robertsson, J.O. & Holliger, K., 1998. Finite-difference modeling of electromagnetic wave propagation in dispersive and attenuating media, *Geophysics,* **63**(3), 856–867.

Birchak, J.R., Gardner, C.G., Hipp, J.E. & Victor, J.M., 1974. High dielectric constant microwave probes for sensing soil moisture, *Proc. IEEE,* **62**(1), 93–98.

Bohlen, T., 2002. Parallel 3-D viscoelastic finite difference seismic modelling, *Comput. Geosci.,* **28**(8), 887–899.

Boiero, D. & Socco, L.V., 2014. Joint inversion of Rayleigh-wave dispersion and P-wave refraction data for laterally varying layered models, *Geophysics,* **79**(4), EN49–EN59.

Boniger, U. & Tronicke, J., 2010. On the potential of kinematic GPR surveying using a self-tracking total station: evaluating system crosstalk and latency, *IEEE Trans. Geosci. Remote Sens.,* **48**(10), 3792–3798.

Booth, A.D., Clark, R. & Murray, T., 2010. Semblance response to a ground-penetrating radar wavelet and resulting errors in velocity analysis, *Near Surf. Geophys.,* **8**(3), 235–246.

Bradford, J.H. & Deeds, J.C., 2006. Ground-penetrating radar theory and application of thin-bed offset-dependent reflectivity, *Geophysics,* **71**(3), K47–K57.

Bradford, J.H., Clement, W.P. & Barrash, W., 2009. Estimating porosity with ground-penetrating radar reflection tomography: a controlled 3-D experiment at the Boise Hydrogeophysical Research Site, *Water Resour. Res.,* **45**(4), doi:10.1029/2008WR006960.

Bunks, C., Saleck, F.M., Zaleski, S. & Chavent, G., 1995. Multiscale seismic waveform inversion, *Geophysics,* **60**(5), 1457–1473.

Constable, S.C., Parker, R.L. & Constable, C.G., 1987. Occam's inversion: a practical algorithm for generating smooth models from electromagnetic sounding data, *Geophysics,* **52**(3), 289–300.

Day-Lewis, F.D., Singha, K. & Binley, A.M., 2005. Applying petrophysical models to radar travel time and electrical resistivity tomograms: Resolution-dependent limitations, *J. geophys. Res.,* **110**(B8), doi:10.1029/2004JB003569.

Doetsch, J., Linde, N., Coscia, I., Greenhalgh, S.A. & Green, A.G., 2010. Zonation for 3D aquifer characterization based on joint inversions of multimethod crosshole geophysical data, *Geophysics,* **75**(6), G53–G64.

Doetsch, J., Krietsch, H., Schmelzbach, C., Jalali, M., Gischig, V., Villiger, L., Amann, F. & Maurer, H., 2020. Characterizing a decametre-scale granitic reservoir using ground-penetrating radar and seismic methods, *Solid Earth,* **11**(4), 1441–1455.

Dokter, E., Köhn, D., Wilken, D., De Nil, D. & Rabbel, W., 2017. Full waveform inversion of SH-and Love-wave data in near-surface prospecting, *Geophys. Prospect.,* **65,** 216–236.

Domenzain, D., Bradford, J. & Mead, J., 2020. Joint inversion of full-waveform ground-penetrating radar and electrical resistivity data: Part 1, *Geophysics,* **85**(6), H97–H113.

Domenzain, D., Bradford, J. & Mead, J., 2022. Joint full-waveform ground-penetrating radar and electrical resistivity inversion applied to field data acquired on the surface, *Geophysics,* **87**(1), K1–K17.

Everett, M.E., 2013. *Near-Surface Applied Geophysics,* Cambridge Univ. Press.

Ewing, R. & Hunt, A., 2006. Dependence of the electrical conductivity on saturation in real porous media, *Vadose Zone J.,* **5**(2), 731–741.

Fabien-Ouellet, G., Gloaguen, E. & Giroux, B., 2017. Time domain viscoelastic full waveform inversion, *J. geophys. Int.,* **209**(3), 1718–1734.

Feng, D., Cao, C. & Wang, X., 2019. Multiscale full-waveform dual-parameter inversion based on total variation regularization to on-ground GPR data, *IEEE Trans. Geosci. Remote Sens.,* **57**(11), 9450–9465.

Feng, D., Li, B., Wang, X., Ding, S., Tai, X., Cai, L. & Su, X., 2023. An efficient dual-parameter full waveform inversion for GPR data using data encoding, *IEEE Trans. Geosci. Remote Sens.,* **61,** 1–11.

Feng, X., Ren, Q. & Liu, C., 2017. Quantitative imaging for civil engineering by joint full waveform inversion of surface-based GPR and shallow seismic reflection data, *Construct. Build. Mater.,* **154,** 1173–1182.

Forbriger, T., Groos, L. & Schäfer, M., 2014. Line-source simulation for shallow-seismic data. Part 1: theoretical background, *J. geophys. Int.,* **198**(3), 1387–1404.

Gallardo, L.A. & Meju, M.A., 2003. Characterization of heterogeneous near-surface materials by joint 2D inversion of dc resistivity and seismic data, *Geophys. Res. Lett.,* **30**(13), doi:10.1029/2003GL017370.

Gallardo, L.A. & Meju, M.A., 2011. Structure-coupled multiphysics imaging in geophysical sciences, *Rev. Geophys.,* **49**(1), doi:10.1029/2010RG000330.

Gao, L., Pan, Y. & Bohlen, T., 2020. 2-D multiparameter viscoelastic shallow-seismic full-waveform inversion: reconstruction tests and first field-data application, *J. geophys. Int.,* **222**(1), 560–571.

Gao, Y., Tilmann, F., van Herwaarden, D.-P., Thrastarson, S., Fichtner, A., Heit, B., Yuan, X. & Schurr, B., 2021. Full waveform inversion beneath the central Andes: insight into the dehydration of the Nazca slab

and delamination of the back-arc lithosphere, *J. geophys. Res.,* **126**(7), e2021JB021984.

Gassmann, F., 1951. Elasticity of porous media, *Vierteljahrsschrder Naturforschenden Gesselschaft,* **96,** 1–23.

Ghose, R. & Slob, E., 2006. Quantitative integration of seismic and GPR reflections to derive unique estimates for water saturation and porosity in subsoil, *Geophys. Res. Lett.,* **33**(5), doi:10.1029/2005GL025376.

Groos, L., Schäfer, M., Forbriger, T. & Bohlen, T., 2014. The role of attenuation in 2D full-waveform inversion of shallow-seismic body and Rayleigh waves, *Geophysics,* **79**(6), R247–R261.

Heincke, B., Jegen, M., Moorkamp, M., Hobbs, R.W. & Chen, J., 2017. An adaptive coupling strategy for joint inversions that use petrophysical information as constraints, *J. appl. Geophys.,* **136,** 279–297.

Hu, Q., Keating, S., Innanen, K.A. & Chen, H., 2021. Direct updating of rock-physics properties using elastic full-waveform inversion, *Geophysics,* **86**(3), MR117–MR132.

Huang, Y. & Schuster, G.T., 2012. Multisource least-squares migration of marine streamer and land data with frequency-division encoding, *Geophys. Prospect.,* **60,** 663–680 .

Huang, Y., Moorkamp, M., Gao, J. & Zhang, H., 2023. Seismogenic structure of the 2014 M6.5 Ludian earthquake from three-dimensional joint inversion of magnetotelluric data and seismic arrival times, *J. geophys. Res.,* **128**(7), e2022JB026151.

Irnaka, T., Brossier, R., Métivier, L., Bohlen, T. & Pan, Y., 2022. 3-D multicomponent full waveform inversion for shallow-seismic target: Ettlingen Line case study, *J. geophys. Int.,* **229**(2), 1017–1040.

Irving, J. & Knight, R., 2006. Numerical modeling of ground-penetrating radar in 2-D using MATLAB, *Comput. Geosci.,* **32**(9), 1247–1258.

Jordi, C., Doetsch, J., Günther, T., Schmelzbach, C., Maurer, H. & Robertsson, J.O., 2020. Structural joint inversion on irregular meshes, *J. geophys. Int.,* **220**(3), 1995–2008.

Köhn, D., De Nil, D., Kurzmann, A., Przebindowska, A. & Bohlen, T., 2012. On the influence of model parametrization in elastic full waveform tomography, *J. geophys. Int.,* **191**(1), 325–345.

Killingbeck, S. *et al.*, 2020. Integrated borehole, radar, and seismic velocity analysis reveals dynamic spatial variations within a firn aquifer in southeast Greenland, *Geophys. Res. Lett.,* **47**(18), e2020GL089335.

Klotzsche, A., Vereecken, H. & van der Kruk, J., 2019. Review of crosshole ground-penetrating radar full-waveform inversion of experimental data: Recent developments, challenges, and pitfalls, *Geophysics,* **84**(6), H13–H28.

Krebs, J.R., Anderson, J.E., Hinkley, D., Neelamani, R., Lee, S., Baumstein, A. & Lacasse, M.-D., 2009. Fast full-wavefield seismic inversion using encoded sources, *Geophysics,* **74**(6), WCC177–WCC188.

Lan, T., Liu, N., Han, F. & Liu, Q.H., 2018. Joint petrophysical and structural inversion of electromagnetic and seismic data based on volume integral equation method, *IEEE Trans. Geosci. Remote Sens.,* **57**(4), 2075–2086.

Leong, Z.X. & Zhu, T., 2021. Direct velocity inversion of ground penetrating radar data using GPRNet, *J. geophys. Res.,* **126**(6), e2020JB021047.

Levander, A.R., 1988. Fourth-order finite-difference P-SV seismograms, *Geophysics,* **53**(11), 1425–1436.

Linde, N. & Doetsch, J., 2016. Joint inversion in hydrogeophysics and near-surface geophysics, in *Integrated Imaging of the Earth: Theory and Applications,* pp. 117–135, eds Moorkamp, M., Lelièvre, P. G., Linde, N. & Khan, A., Wiley.

Linde, N. & Doetsch, J.A., 2010. Joint inversion of crosshole GPR and seismic traveltime data, in *Advances in Near-surface Seismology and Ground-penetrating Radar,* Chapter 1, pp. 1–18, eds Miller, Richard D., Bradford, John H. & Holliger, Klaus, Society of Exploration Geophysicists, American Geophysical Union, Environmental and Engineering Geophysical Society.

Linde, N., Binley, A., Tryggvason, A., Pedersen, L.B. & Revil, A., 2006. Improved hydrogeophysical characterization using joint inversion of crosshole electrical resistance and ground-penetrating radar traveltime data, *Water Resour. Res.,* **42**(12), doi:10.1029/2006WR005131.

Linde, N., Tryggvason, A., Peterson, J.E. & Hubbard, S.S., 2008. Joint inversion of crosshole radar and seismic traveltimes acquired at the South Oyster Bacterial Transport Site, *Geophysics,* **73**(4), G29–G37.

Liu, X., Zhu, T. & Hayes, J., 2022a. Critical zone structure by elastic full waveform inversion of seismic refractions in a sandstone catchment, central Pennsylvania, USA, *J. geophys. Res.,* **127**(3), e2021JB023321.

Liu, Y., Irving, J. & Holliger, K., 2022b. High-resolution velocity estimation from surface-based common-offset GPR reflection data, *J. geophys. Int.,* **230**(1), 131–144.

Meles, G.A., Van der Kruk, J., Greenhalgh, S.A., Ernst, J.R., Maurer, H. & Green, A.G., 2010. A new vector waveform inversion algorithm for simultaneous updating of conductivity and permittivity parameters from combination crosshole/borehole-to-surface GPR data, *IEEE Trans. Geosci. Remote Sens.,* **48**(9), 3391–3407.

Mollaret, C., Wagner, F.M., Hilbich, C., Scapozza, C. & Hauck, C., 2020. Petrophysical joint inversion applied to alpine permafrost field sites to image subsurface ice, water, air, and rock contents, *Front. Earth Sci.,* **8,** doi:10.3389/feart.2020.00085.

Moorkamp, M., 2022. Deciphering the state of the lower crust and upper mantle with multi-physics inversion, *Geophys. Res. Lett.,* **49**(9), e2021GL096336.

Moran, M.L., Greenfield, R.J., Arcone, S.A. & Delaney, A.J., 2000. Multidimensional GPR array processing using Kirchhoff migration, *J. appl. Geophys.,* **43**(2), 281–295.

Nur, A., 1992. Critical porosity and the seismic velocities in rocks, *EOS, Trans. Am. geophys. Un.,* **73,** 43–66.

Pan, Y., Gao, L. & Bohlen, T., 2019. High-resolution characterization of near-surface structures by surface-wave inversions: from dispersion curve to full waveform, *Surv. Geophys.,* **40**(2), 167–195.

Pan, Y., Gao, L. & Bohlen, T., 2021. Random-objective waveform inversion of 3D-9C shallow-seismic field data, *J. geophys. Res.,* **126**(9), e2021JB022036.

Qin, T., 2022. Full-waveform inversion of ground-penetrating radar data and its indirect joint petrophysical inversion with shallow-seismic data, *PhD thesis*, Karlsruhe Institute of Technology.

Qin, T., Bohlen, T. & Pan, Y., 2022. Indirect joint petrophysical inversion of synthetic shallow-seismic and multi-offset ground-penetrating radar data, *J. geophys. Int.,* **229**(3), 1770–1784.

Qin, T., Bohlen, T. & Allroggen, N., 2023. Full-waveform inversion of ground-penetrating radar data in frequency-dependent media involving permittivity attenuation, *J. geophys. Int.,* **232**(1), 504–522.

Revil, A., 2013. Effective conductivity and permittivity of unsaturated porous materials in the frequency range 1 mHz–1GHz, *Water Resour. Res.,* **49**(1), 306–327.

Romero-Ruiz, A., Linde, N., Keller, T. & Or, D., 2018. A review of geophysical methods for soil structure characterization, *Rev. Geophys.,* **56**(4), 672–697.

Schäfer, M., Groos, L., Forbriger, T. & Bohlen, T., 2014. Line-source simulation for shallow-seismic data. Part 2: full-waveform inversion'a synthetic 2-D case study, *J. geophys. Int.,* **198**(3), 1405–1418.

Sun, J., Innanen, K., Zhang, T. & Trad, D., 2023. Implicit seismic full waveform inversion with deep neural representation, *J. geophys. Res.,* **128**(3), e2022JB025964.

Tarantola, A., 1984. Inversion of seismic reflection data in the acoustic approximation, *Geophysics,* **49**(8), 1259–1266.

Tikhonov, A.N. & Arsenin, V.Y., 1977. *Solutions of Ill-Posed Problems,* V.H. Winston.

Topp, G.C., Davis, J.L. & Annan, A.P., 1980. Electromagnetic determination of soil water content: Measurements in coaxial transmission lines, *Water Resour. Res.,* **16**(3), 574–582.

Wagner, F.M. & Uhlemann, S., 2021. An overview of multimethod imaging approaches in environmental geophysics, *Adv. Geophys.,* **62,** 1–72.

Wagner, F.M., Mollaret, C., Günther, T., Kemna, A. & Hauck, C., 2019. Quantitative imaging of water, ice and air in permafrost systems through petrophysical joint inversion of seismic refraction and electrical resistivity data, *J. geophys. Int.,* **219**(3), 1866–1875.

Wang, T., Cheng, J. & Geng, J., 2021. Reflection full waveform inversion with second-order optimization using the adjoint-state method, *J. geophys. Res.,* **126**(8), e2021JB022135.

Wittkamp, F., Athanasopoulos, N. & Bohlen, T., 2019. Individual and joint 2-D elastic full-waveform inversion of Rayleigh and Love waves, *J. geophys. Int.,* **216**(1), 350–364.

Xia, J., Miller, R.D. & Park, C.B., 1999. Estimation of near-surface shear-wave velocity by inversion of Rayleigh waves, *Geophysics,* **64**(3), 691–700.

Xia, J., Xu, Y., Luo, Y., Miller, R.D., Cakir, R. & Zeng, C., 2012. Advantages of using multichannel analysis of Love waves (MALW) to estimate near-surface shear-wave velocity, *Surv. Geophys.,* **33**(5), 841–860.

Xu, L., Winner, V. & Maurer, H., 2023. Gradient-constrained model parametrization in 3-D compact full waveform inversion, *J. geophys. Int.,* **232**(1), 366–397.